The SERCA residue Glu340 mediates inter-domain communication that guides Ca^{2+} transport

Johannes D. Clausen[1,2*], Bertrand Arnou[1,3*], Maxwell M. G. Geurts[4*], Cedric Montigny[3], Guillaume Lenoir[3], Robin A. Corey[4], Christine Jaxel[3], Jesper V. Møller[1], Poul Nissen[2], Jens Peter Andersen[1], Marc le Maire[3], Maike Bublitz[2,4#]

[1]Department of Biomedicine, Aarhus University, Ole Worms Allé, 8000 Aarhus C, Denmark

[2]Department of Molecular Biology and Genetics, Aarhus University, Gustav Wieds Vej 10c, 8000 Aarhus C, Denmark

[3]Université Paris-Saclay, CEA, CNRS, Institute for Integrative Biology of the Cell (I2BC), 91198 Gif-sur-Yvette, France.

[4]Department of Biochemistry, University of Oxford, South Parks Road, Oxford OX1 3QU, United Kingdom

[5]Danish Research Institute of Translational Neuroscience – DANDRITE, Nordic EMBL Partnership for Molecular Medicine

*these authors contributed equally

[#]To whom correspondence should be addressed: maike.bublitz@bioch.ox.ac.uk

Running title: The E340A mutant of SERCA

Abstract

The sarco(endo)plasmic reticulum Ca^{2+}-ATPase (SERCA) transports Ca^{2+} ions from the cytosol into the SR/ER lumen. SERCA's activity is dependent on a tight coupling between movements of the transmembrane helices that comprise the two Ca^{2+} binding sites and the cytosolic ATPase headpiece. We have addressed the molecular basis for this intramolecular communication by analysing the structure and functional properties of the SERCA mutant E340A. The conserved residue Glu340 is located at a strategic position in the ATPase, at the interface between the phosphorylation domain and the cytosolic ends of six out of SERCA's ten transmembrane helices. The mutant displays a reduced rate of binding Ca^{2+} ions from the cytosol. The structure of E340A reveals a rotated headpiece, altered connectivity between the cytosolic domains and an altered interaction pattern around the mutated residue Glu340. Supported by molecular dynamics simulations, we conclude that the E340A mutation causes a stabilisation of SERCA in a more occluded state, causing slowed dynamics in the ion binding region. This finding underpins the crucial role of Glu340 in the inter-domain communication of SERCA.

Keywords

Ca^{2+} binding / P-type ATPase / SERCA / Tryptophan fluorescence / Molecular Dynamics Simulations

Introduction

The Ca^{2+}-ATPase of sarco(endo)plasmic reticulum (SERCA) is an ion-translocating ATPase of the P-type family. It translocates cytosolic Ca^{2+} ions across the sarco- or endoplasmic reticulum membrane at the expense of ATP, a vital function in all living cells, particularly in the context of muscle contraction, Ca^{2+} signalling and cell survival[1].

The molecular Ca^{2+} transport mechanism of SERCA is based on a cyclic transition through different conformations of the 110 kDa membrane protein, allowing alternating access to the Ca^{2+} binding sites from the cytosol and the SR/ER lumen. Binding and hydrolysis of ATP is mediated by SERCA's cytosolic 'headpiece' which consists of three roughly globular domains, the nucleotide-binding (N), phosphorylation (P), and actuator (A) domain, while the Ca^{2+} binding sites are located in the transmembrane part of the protein (Fig 1A). ATP binding and a subsequent transient phosphorylation of a conserved aspartate residue is coupled to a sequence of binding of two Ca^{2+} ions from the cytosol, occlusion, and luminal release of these ions. This is associated with conformational transitions between so-called *E*1, *E*1P, *E*2P and *E*2 forms, where 'P' represents phosphorylation (Fig 1B)[1,2].

Both the P and the A domain of the cytosolic headpiece are in contact with the ten-transmembrane (TM-) helical domain, albeit by different structural elements: the A domain is connected via three loops (A-M1, M2-A and A-M3) that are thought to relay the movements of the A domain to the M1-M3 helices. The P domain however, is structurally very tightly integrated into the cytosolic ends of M4 and M5. M4 is linked to the so-called P1 helix, a short α-helix that runs roughly parallel to the membrane

surface, at the membrane-facing side of the P-domain. P1 is a key element of inter-domain communication: it connects directly to a β-strand ending with the phosphorylated aspartate residue, and it makes contact to the cytosolic end of M3 and to the loop between M6 and M7 (L6-7), which has been shown to play an important role in SERCA catalysis [3–9]. (Fig 1A).

There are two ion-binding sites within the TM domain of SERCA, denoted sites I and II based on a proven sequential order of Ca^{2+} binding. The Ca^{2+} coordination in site I is mediated by residues in helices M5, M6, and M8, and in site II by residues in M4 and M6. The transition from the *E*1P to the *E*2P state is associated with a large rotation of the A domain, which causes a distortion of the coordination geometry at the high-affinity Ca^{2+}-binding sites and a concomitant loss of Ca^{2+} affinity, along with a formation of a luminal exit pathway for Ca^{2+} release. A number of crystal structures have shed light on the nature of the conformational changes associated with Ca^{2+} transport (reviewed in [10,11]). Ca^{2+} binding to SERCA involves the characteristically kinked M1 helix (Fig 1A). A large vectorial movement of M1 toward the luminal side of the membrane mediates Ca^{2+} access from the cytosolic side, whereas Ca^{2+} occlusion after binding depends on a M1 movement in the opposite direction, allowing the formation of a hydrophobic cluster around the kink that shields the Ca^{2+} sites. This goes along with a smaller 'upward' shift of M3 relative to M5 (by about half a helix winding) [12,13].

Glu340, a centrally positioned residue in the P1 helix (Pro337-Cys344) (Fig 1A), is almost universally conserved among P-type ATPases [14] and appears to play a key role in linking the P and the TM domains. The specific functional role of Glu340 has been studied thoroughly with an E340A SERCA mutant produced in COS cells [9]. The mutation causes a very pronounced slowing of two related partial reactions, namely H_n*E*2 -> *E*1 -> Ca_2*E*1 (proton release, Ca^{2+} binding and the associated conformational change) and the reverse reaction Ca_2*E*1 -> *E*1 (Ca^{2+} dissociation from the high affinity sites towards the cytosol). It does, however, not affect SERCA's apparent vanadate affinity (which is typically affected by *E*2-*E*1 shifts), suggesting that the inhibition of H_n*E*2 -> *E*1 -> Ca_2*E*1 affects the latter part of this reaction step (i.e. actual Ca^{2+} binding). The mutation does not significantly affect the remaining partial reaction steps of the cycle. Hence, Glu340 seems to be specifically critical for the partial reactions involving cytoplasmic Ca^{2+} interactions. This likely relates to its central position in the structure (Fig 1A), suggesting that communication between the membranous Ca^{2+} binding sites and the cytosolic phosphorylation site is critical for the conformational changes involved in Ca^{2+} binding.

Structural information on SERCA mutants is highly valuable for understanding its transport cycle, but it is relatively scarce with only four published crystal structures to date [15–17]. The main reason for this shortage is that purification and crystallization of recombinantly produced SERCA is challenging, with low protein yields and poor stability in the absence of native lipids compared to the native enzyme purified from skeletal muscle.

In this study, we have succeeded in determining the crystal structure of yeast-expressed rabbit SERCA1a mutant E340A at 3.2 Å in the Ca_2*E*1 form with bound ATP analogue (AMPPCP), and we have collected biochemical data on the protein's ATPase activity and Ca^{2+} binding/dissociation dynamics. This is notably the first structure of a SERCA mutant that is catalytically active, *i.e.* capable of completing a full catalytic cycle, albeit with altered kinetics. We have furthermore run a series of

molecular dynamics (MD) simulations of both wild-type (WT) and E340A structures embedded in a lipid bilayer. The functional and structural features of E340A in comparison with the WT are discussed below, linking the structure to Glu340's functional importance and providing important insight into the inter-domain communication that guides Ca^{2+} transport by SERCA.

Results and Discussion

SERCA E340A has a lower ATPase activity and slower Ca^{2+} binding kinetics than WT

Prior studies have investigated the effect of the E340A mutation in microsomes derived from mammalian cells [6,9] and found a reduced ATPase activity compared to WT. In order to assess whether the mutation has a similar effect on the solubilized yeast-expressed SERCA, we used an enzyme-coupled assay to estimate the specific activity of the E340A mutant. We observed that the ATPase activity of the E340A mutant is about 25 % of the WT (0.86 vs. 3.45 µmoles ATP/mg/min, n=9) (Fig 1C, Appendix FigS1), *i.e.* a marked slowing of the enzyme cycle similar to, although not as extensive as that reported in prior studies (11-13 %) [6,9]. However, in the previous experiments, activity was measured in microsomal membranes, at pH 7.0. Here, we measured ATPase activity of DDM-solubilized and purified enzyme at pH 7.5 and in the presence of a large excess of $C_{12}E_8$, a mild detergent that has been described to stabilize SERCA1a during turn-over [18]. The presence of detergent has been shown to accelerate specifically the *E*2 → Ca_2*E*1 transition, providing a likely explanation for the less drastic effect of the E340A mutation observed here [18,19].

In order to assess the time course of the Ca^{2+} binding transition for the yeast-expressed SERCA E340A, we measured the changes in intrinsic tryptophan fluorescence upon addition of Ca^{2+} to the *E*2 state of the protein. The *E*2 to Ca_2*E*1 transition of E340A is significantly slower than that of the WT, with an increase of $t_{1/2}$ of about 3-fold (Fig 1D-F), i.e. again a qualitatively similar effect, although not as dramatic, as the 40-fold increase reported by Clausen *et al.* [9]. Again, the earlier experiments were done with microsomes while here it was done on detergent-solubilized purified ATPases, *i.e.* in conditions described to significantly accelerate this transition [19].

In conclusion, the functional measurements on our soluble yeast-expressed E340A mutant exhibits functional properties qualitatively similar to those previously described for the membrane bound mutant [9], albeit with quantitative differences in the observed rate constants referable to the detergent solubilized state of the enzyme prepared for crystallization.

The mutation E340A causes global changes in SERCA's domain arrangement

Our crystal structure of SERCA E340A at 3.2 Å resolution (Fig 1A, Table 1) allows for a detailed structural comparison with the WT structure. When superposed, the WT and E340A structures deviate by a substantial RMSD of 2.3 Å over all main chain atoms. Nevertheless, when superposed on the C-terminal transmembrane helix bundle M5-M10 (residues 750-994, main chain RMSD= 0.49 Å), the E340A mutant and WT have

an almost identical arrangement of the remaining transmembrane helices M1-M4 (main chain RMSD = 0.56 Å), with a small 1.6 Å bend at the cytosolic end of M3 in E340A (Fig 2A), and a slightly more kinked helix M1 (105° in E340A vs. 109° in WT). In line with this, the Ca^{2+} binding sites look identical in WT and E340A. This indicates that the difference in the Ca^{2+} binding and dissociation dynamics between WT and E340A are not caused by a perturbation of the geometry at the Ca^{2+} sites at the TM domain but rather by altered kinetics of the actual binding process.

In contrast to the almost identical arrangement in the TM domain, there is a pronounced shift (ca 10 Å) in the position of the cytosolic headpiece, which is rotated further 'downward' towards the membrane surface in E340A (Fig 2A and Movie EV1). The pivot points of this headpiece movement are at the cytosolic ends of M2, M4 and M5. Whereas M2 and M4 stay very rigid throughout their entire lengths, M5 undergoes a slight bend in the region between its C-terminal end (at Phe740), which is embedded in the P-domain, up till residue Gly750, which sits at the 'rear side' of P1, exactly opposite residue 340. On the 'front side' of P1, the N-terminal end of M3 moves in the opposite direction of the shifting P1 helix, bending slightly inwards with its first two N-terminal windings. (Fig 2A insert, Movie EV1).

Intriguingly, the downward rotation of the cytosolic headpiece in E340A is an extension of exactly the same trajectory as the movement of WT SERCA when it shifts from empty Mg*E*1 to the Ca^{2+}-bound *E*1 form (Ca_2*E*1): when Ca^{2+} binds to WT SERCA, the entire P1-M3 network moves upwards relative to L6-7 and M5, by about 4.5 Å, while the overall headpiece rotates down towards the membrane surface [13]. In E340A, this headpiece downward rotation continues further by about 10 Å (as visualised in a superposed morph between the Mg*E*1 (PDB 4H1W) and the Ca_2*E*1 WT (PDB 3N8G) and E340A (PDB 6RB2) structures, see Movie EV2. This extension of the WT Ca^{2+}-binding trajectory is reflected in a larger main chain RMSD between the empty WT structure and the Ca^{2+}-bound states in E340A (5.6 Å) than in WT SERCA (4.7 Å).

The observation of an 'overshooting' Ca^{2+}-binding movement in E340A led us to ask whether this mutation might lead to a stabilisation of a Ca^{2+} occluded state, the state that follows Ca^{2+}- (and nucleotide) binding in the catalytic cycle. Ca^{2+} occlusion is normally stabilised by the initiation of ATP hydrolysis and not by Ca^{2+} binding alone [12]. We hence looked at further structural deviations of SERCA E340A in more detail, starting at the contacts between the three domains of the cytosolic headpiece (N, P, and A domains).

Connectivity between the N- and A domains is looser in E340A

While the domain bodies themselves do not change between WT and E340A (main chain RMSD of 0.37 Å, 0.37 Å and 0.32 Å for the single P-, N-, and A domains, respectively), their concerted movement relative to the rest of the structure in E340A is reflected by an overall main chain RMSD for the entire headpiece of 1.16 Å. The P- and the N domain appear to move together as one rigid body (main chain RMSD = 0.47 Å for the P/N body), whereas the A domain gets displaced slightly further, with the distance between the N- and the A domain increasing by approx. 3 Å in the final position. The main chain RMSD of 1.4 Å for the N/A body is the largest RMS deviation measured for any element of the two structures, indicating that this is the largest structural change induced by the mutation. This change leads to the loss of 6 out of 8 polar contacts between the N- and the A domain (Arg134 to Phe427, Arg139 to Asp426 and Glu435, Lys169 to Thr484, Thr171 to Leu578, and Lys218 to Asp422), leaving only two contacts intact between these two domains (Arg134 to Asp426 and Thr171 to Glu486), whereas the A domain's contacts to the P domain remain intact (Gly156 to Ala725 and Val726, Asn213 to Thr729) (Fig 2B and C). This loss of N-A contacts is also evident from our MD simulations (see below and Fig 3C).

Local changes at the mutated residue 340

In the Ca_2E1 form of WT SERCA (PDB 3N8G), the Glu340 side chain is in hydrogen bonding distance to the side chain OH group of Thr247 and the main chain nitrogen of Leu249 at the N-terminal end of M3, with additional electrostatic attraction by the partial positive charge of the helix N terminus. A third interaction of Glu340 is a water-mediated contact to Arg822 in L6-7 (Fig 2D).

Interestingly, the local conformation around the Glu → Ala mutation (within a radius of ~ 10 Å) is very similar to WT, with measurable shifts of under 2 Å (Fig 2A and D-E). While the local similarity may seem surprising at first glance, looking at the larger global structural changes described above, it becomes clear that residue A340 is located very close to the pivot point for the described headpiece rotation and therefore does not move much itself.

The overall distance between P1 and M3 is slightly closer than in WT, and the nature of the contact between these two structural elements is very different in E340A: there are no apparent polar interactions between P1 and M3, except for a distant (4.4 Å) contact between Thr341 in P1 and Thr247 in M3 (Fig 2E). Instead, the electrostatic attraction to the partially positive M3 N terminus is replaced with hydrophobic interactions (Ala340 to Leu249, Pro337 to the methyl group of Thr247, and Thr341 to Pro248). In fact, this interaction appears to be rather tight, as shown by our MD simulations (see below and Fig 3B). In this context it is interesting to note that a mutation of Leu249 at the tip of M3 to alanine leads to increased rates of both Ca^{2+} binding and dissociation [20].

Removal of the Glu340 side chain abolishes the contact to Arg822, and the entire L6-7 loop (Phe809 to Ser830) gets displaced laterally by ca. 3 Å, increasing the distance between Arg822 and the P1 helix. Prior studies have implicated an important role of L6-7 in SERCA catalysis [8,9,20]. For example, the D813A-D818A mutation leads to a dramatic loss of Ca^{2+} affinity [8]. There are also striking similarities between the behaviour of the mutant E340A and some L6-7 mutants [9]. The loop has moreover

been suggested to be part of an ion access pathway in both SERCA and the Na^+/K^+-ATPase [4,5,7,8,21], and/or to contribute to the coordination of events between the cytosolic and transmembrane domains [6,8,9]. In light of these findings, we hypothesised that the loss of the Arg822-Glu340 contact in E340A contributes to the functional impairment of this mutation. In order to further test this hypothesis, and to validate the structural and functional differences between WT and E340A described above, we conducted molecular dynamics (MD) simulations.

Molecular Dynamics Simulations support a more occluded state of E340A

In order to assess whether the differences we found between the crystal structures of WT SERCA and E340A might reflect stable conformations occurring in the native membrane environment, and to find further explanations for the observed functional impairment of the mutant, we carried out 3 x 200 ns of all-atom MD simulations of each structure reconstituted in a POPC lipid bilayer. As an internal control, we generated an *in silico* mutant $E340A_{is}$ by truncation of the Glu340 side chain from the WT Ca_2E1 structure and subjected it to the same simulations.

To quantify the conformational downward shift of the cytosolic headpiece relative to the membrane, we determined the angle between three points; Leu13 in the A domain and Thr86 and Leu98 in M2 (Fig EV1A). When comparing the two crystal structures, the angle in E340A is 5° more acute (147°) than in WT (152°). During the course of the simulations, both structures relax towards more acute angles, but the difference between them stays about the same, with E340A having a median angle of 142° and WT of 146° (Fig 3A). This confirms that the difference in headpiece angle is a true feature of E340A that persists in a dynamic membrane environment.

Coherent with the above finding, the P1 helix remains closer to the tip of M3 in E340A, as shown by the distance between the C_α-atoms of residue 340 and Leu249 at the tip of M3 (Figs 3B and EV1B). The WT structure exhibits a bimodal distribution of distances with peaks at 7.5 Å and 8.8 Å, whereas E340A has a prominent peak at a shorter distance than WT (6.9 Å).

The loss of connectivity between the A domain and the N/P-body described above is also apparent from the MD simulations. The number of H-bonds between these elements remains reduced in E340A throughout the simulation (Fig 3C).

In the three analyses described above, the *in silico* mutant $E340A_{is}$ gives similar distributions to WT, likely because the rather large domain movements are too slow to be seen after the short simulation time of 200 ns. This is in accord with the wider spread of values in the E340A*is* histograms, indicating that the artificially mutated structure is still equilibrating after 200 ns. When looking at more local dynamics, however, $E340A_{is}$ does behave more similar to E340A, as seen in the analyses below.

The crystal structure suggests that Glu340 can engage in up to three hydrogen bonds: with Thr247, the backbone of Leu249 and a water-mediated contact to Arg822 (Fig 2D). Mutation of Arg822 had previously been shown to have a similar effect as mutating E340: a slowing of the Ca^{2+}-binding transition from *E*2 and of Ca^{2+} dissociation [9]. The link to Arg822 in L6-7 is completely lost in E340A (Fig 2E). Despite the loss of this ionic contact, there is only a slight displacement of L6-7, which is held in place by contacts to L8-9 and other regions of the P domain. Accordingly, we could

not detect an increased motility of L6-7 in our MD simulations (Fig EV2A). Nevertheless, our simulation data show that – in the absence of the Glu340 side chain – Arg822 can swing out of the site between P1 and M3 (Fig EV2B). This is measurable as a sudden increase in the distance between Arg822 N_ε and Ala340 C_β from about 7 Å to 13 Å in E340A and to more than 14 Å in E340A*is* (Figs 3D and EV2C). In WT SERCA, Arg822 does not swing out spontaneously, and the distance stays at 7-10 Å. (Fig 3D). Importantly, once moved to the 'out' position, Arg822 does not return to the 'in' position over the course of any of our simulations of E340A and $E340A_{is}$ (Figs 3D and EV2C). The outward swing of Arg822 does, however, not lead to a loss of contact between P1, M3 and L6-7, as might be expected at first glance. On the contrary, concomitant with the outward swing of Arg822 from the wedge between P1 and M3, the space is taken up by Leu249 at the tip of M3, which closes in on the gap and approaches Pro824 in the L6-7 loop (Fig 3B and EV2D), reducing the distance between the two Cα atoms from 10 Å (E340A*is*) or 7.5 Å (E340A) to 5 Å (Figs 3D and EV3C). This approach of M3 toward L6-7 is mutually exclusive with the 'in' position of Arg822, as seen by a conspicuous correlation of the distance plots between Arg822 and Ala340 and between Leu249 and Pro824. This correlation is also evident in the *in silico* mutant E340A*is* but absent from the WT (Figs 3D and EV3C), suggesting that the changes in the contact network around P1 play a central role in mediating the observed structural changes in E340A.

Interestingly, we also found a difference in the kinked region of M1 between WT and both E340A and $E340A_{is}$. The kink at Leu60 in M1 has been known since the first *E*2 structure of SERCA was determined [22] and has later also been found in nucleotide-bound *E*1 SERCA structures [12,23]. The kink permits the conserved residue Phe57 to engage in hydrophobic interactions with Val62, Leu65, (both also conserved) and Leu98, a cluster that shields off the Ca^{2+} binding sites as a prerequisite for ion occlusion. We find that M1 is rigidly kinked in E340A, while in WT the kink region displays more dynamics and can straighten to some extent (Figs 3E and EV3). Notably, a straight M1 helix has been seen in nucleotide-free inward-open E1 structures [16,24]), and is associated with an un-occluded Ca_2E1 state of SERCA. Hence, the observed structural changes to both M1 and M3/L6-7 appear to shift E340A towards a slightly more occluded state than WT.

In order to further probe our simulation data with respect to a more occluded state in E340A, we analysed the nucleotide binding site. Ca^{2+} occlusion is coupled to phosphorylation of Asp351, and a more occluded conformation of SERCA would be expected to be more prone to be phosphorylated. We hence compared the distances between the ATP γ-phosphate and the respective closer of the two carboxyl oxygen atoms of Asp351, along with the angles between the carboxyl oxygen and the O-P bond of the terminal phosphoanhydride in ATP (Fig EV4). For comparison, the crystal structure in which the fully occluded transition state of phosphorylation has been trapped with ADP-AlF_x [12] the distance and angle between the Asp351 O_δ and the aluminium atom are 2.1 Å and 159 °, respectively. As seen in Fig 3F**,** the WT structure displays a large spread of angles (between 60 and 180°) and distances (between 3 and 5 Å), many of which are not compatible with an in-line associative hydrolysis mechanism. In E340A, the distances take up a much narrower spread mostly between 3.5 and 4 Å, and the angles are more restricted towards the catalytically competent obtuse region (between 110° and 170°). E340A*is* displays an intermediate distribution. Our data are therefore consistent with a more occluded state in both the ion binding and the nucleotide binding regions of E340A.

Conclusions

The SERCA mutant E340A displays a reduced rate of the Ca^{2+} binding transition, as well as a slower Ca^{2+} dissociation rate [9]. Both the reduced rate of the Ca^{2+} binding transition and the resulting reduction of the Ca^{2+} activated ATPase activity were demonstrated here for the solubilized yeast-expressed SERCA E340A. These kinetics are consistent with the hypothesis that perturbation of the hydrogen-bonding network around Glu340 causes a slowing, in both directions, of the structural changes associated with the binding of the second Ca^{2+} ion to the Ca*E*1 state and the subsequent occlusion step. Moreover, from rapid kinetics experiments of phosphorylation, we know that ATP reacts very well with Ca^{2+}-bound E340A – if not even faster – than with WT [9], suggesting that once formed, the occluded intermediate is more stable in the E340A mutant. How can the slow binding and dissociation of Ca^{2+} and a stabilisation of the occluded state be explained in structural terms? The loss of H-bonds between the A domain and the N/P body in E340A hints at an altered position of the A-domain. At the same time, M3 is associated closely with the P1 helix and L6-7, and M1 is in a more locked kink than WT. Both a rearrangement of the A-domain and a locked M1 kink – indicative of the formation of the hydrophobic cluster adjacent to the Ca^{2+} binding sites – have been postulated to favour Ca^{2+}-occlusion and phosphorylation of Asp351 in SERCA [12,16]. Concurrently, we find the local environment of the catalytic site of E340A more narrowly clustered around a catalytically competent geometry than in WT, thus emphasizing the link between occlusion and phosphorylation.

Taken together, our data suggest that E340A represents a structure that is stabilised in a state closer to occlusion and phosphorylation than the WT structure, hence slowing Ca^{2+} entry and release but favouring phosphorylation by ATP. Conversely it can be concluded that the conserved residue Glu340 in SERCA has an important role in maintaining the structural flexibility needed to allow for rapid Ca^{2+} exchange at the membranous binding sites, and in relaying this flexibility to the site of phosphorylation.

Material and Methods

Chemicals

Octaethylene glycol mono-n-dodecyl ether ($C_{12}E_8$) was purchased from Nikkol Chemical (#BL-8SY; Tokyo, Japan), and n-dodecyl β-D-maltopyranoside (DDM) was from Anatrace (#D310; Maumee, OH). Streptavidin Sepharose high performance resin was provided by GE Healthcare (#17-5113-01; Orsay, France). Thapsigargin (TG stock solution was prepared at 1 mg/mL in DMSO, i.e. about 1.5 mM) was from VWR International (#586005; Fontenay-sous-Bois, France). All other chemical products were purchased from Sigma (Saint-Quentin Fallavier, France). Sequence for SERCA1a heterologous expression was from rabbit.

Cloning, expression and purification

SERCA1a E340A cDNA (SERCA1a[E340A]) was recovered from pMT2 vector initially used for expression in COS cells [9] and cloned into the yeast expression plasmid pYeDP60, with a C-terminal biotin acceptor domain [25], resulting in pYeDP60_SERCA1a[E340A]-Bad. The construct was checked by sequencing (Eurofins MWG). The *Saccharomyces cerevisiae* yeast strain W303.1b/Gal4 (α, leu2, his3, trp1::TRP1-GAL10-GAL4, ura3, ade2–1, canr, cir) was the same as previously described [25]. Transformation was performed according to the lithium acetate/single-stranded carrier DNA/PEG method [26].

Expression and purification of the E340A mutant SERCA1a was done as previously described for the WT (WT) enzyme [25]. Briefly, after overexpression in the yeast *S. cerevisiae*, light membranes were prepared and solubilized by DDM for subsequent purification by Streptavidin affinity chromatography [25,27,28]. Purified WT SERCA1a was recovered in a buffer containing 50 mM MOPS-Tris pH 7, 100 mM KCl, 5 mM $MgCl_2$, 2.1 mM $CaCl_2$, 40 % glycerol (v/v) and 0.5 mg/mL DDM, together with some thrombin remaining from the elution procedure. The protein concentration in the purified fraction was typically in the 0.05 to 0.15 mg/mL range depending on the batch. Further purification for crystallization trials was carried out as described previously for the SERCA E309Q mutant [16], involving exchange of DDM with $C_{12}E_8$ and relipidation of the purified SERCA with DOPC.

ATPase activity measurements

Steady-state ATPase activity measurements were performed using an enzyme-coupled assay by measuring the rate of NADH oxidation (followed by absorbance at 340 nm) in the presence of 0.02 mg/mL lactate dehydrogenase, 0.04 mg/mL pyruvate kinase, 1 mM phosphoenolpyruvate, 0.3 – 0.4 mM NADH, 5 mM MgATP [29] and in the additional presence of 1 mg/mL $C_{12}E_8$ and 50 µM free Ca^{2+} to limit time-dependent inactivation of the SERCA1a [18], at 30°C and pH 7.5.

Tryptophan fluorescence

Intrinsic fluorescence was measured with a Fluorolog spectrofluorimeter (Horiba / Jobin-Yvon, Palaiseau, France), in a temperature-regulated and continuously stirred 2 mL quartz cuvette. Excitation and emission wavelengths were set at 295 and 320 nm, with bandwith of 2 and 5 nm, respectively. Integration time for recording of the signal was 2 seconds. SERCA1a intrinsic fluorescence changes were measured with purified WT or purified E340A mutant suspended at a protein concentration of about 10 µg/mL in a buffer containing 50 mM Mes-Tris pH 6.5, 5 mM $MgCl_2$, 20% glycerol

(v/v) and 2 mg/mL DDM, at 20°C. Initial Ca^{2+} concentration was adjusted to 105 µM on top of the contaminating Ca^{2+} (3 - 5µM) already present in the buffer. This was followed by the addition of 5 mM EGTA (EG), reducing $[Ca^{2+}]_{free}$ to about 100 nM. An extra addition of 12.5 mM $CaCl_2$ (Ca) allowed to reach a final $[Ca^{2+}]_{free}$ of about 7.6 mM. to recover the initial level of fluorescence. Data were fitted with the GraphPad Prism program with an exponential two phase association law on the first 60 seconds of the raw data following Ca^{2+} addition.

Crystallization

Purified SERCA E340A at a concentration of 8-10 mg/ml was supplemented with Ca^{2+}, Mg^{2+}, and AMPPCP to 10, 3, and 1 mM, respectively, and crystallization trials were carried out using the vapour diffusion technique. The crystallization drops were prepared as 1 µl sitting drops, with each drop containing a 1:1 mixture of the concentrated, DOPC-relipidated, and $C_{12}E_8$-solubilized Ca^{2+}-ATPase solution and the reservoir solution. Diffraction-quality crystals were obtained with reservoir solutions containing 200 mM lithium acetate, 18-22% PEG6K, 6-9% glycerol, and 3% tert-butanol. The E340A crystals varied markedly in appearance from crystals obtained with WT under similar conditions. Hence, the E340A crystals displayed a rectangular stick morphology, whereas WT crystals were diamond shaped (cf. Fig S2 in [16]).

Data collection, processing and refinement

Crystals were flash frozen and tested at the microfocus beam line ID23-2 at ESRF. The best dataset diffracted to 3.2 Å. In accordance with the variant crystals form, also the space group and unit cell parameters were different from WT SERCA. Hence, WT crystallizes in space group C2 with unit cell parameters (163 Å, 76 Å, 151 Å, 90°, 109°, 90°), and E340A in space group $P2_12_12$ with unit cell parameters (126 Å, 232 Å, 50 Å, 90°, 90°, 90°), which are hitherto unknown parameters for SERCA. Phasing was done by molecular replacement with the Ca_2E1-AMPPCP form (1T5S). Initial rigid-body refinement with each domain as a single rigid body was followed by all-atom and TLS refinement in *PHENIX* [30].

Molecular graphics figures were prepared with PyMOL [31] and morphs with Morphinator [32].

Molecular Dynamics Simulations

Simulations were built using the coordinates from PDB 3N8G (WT) and 6RB2 (E340A). The protein atoms were described using the CHARMM36 force field [33], and were built into a lipid bilayer composed of POPC molecules and solvated with TIP3P water and Na^+ and Cl^- to 150 mM in a 120 x 120 x 180 Å box. Systems were built using CHARMM-GUI [34,35]. Generation of the *in silico* mutant $E340A_{is}$, was done with CHARMM-GUI.
The systems were energy minimized using the steepest descent method, then equilibrated with positional restraints on heavy atoms for 100 ps in the NPT ensemble at 310 K with the V-rescale thermostat and semi-isotropic Parrinello-Rahman pressure coupling [36,37]. Production simulations were run in triplicate without positional restraints, with 2 fs time steps for a minimum of 200 ns.

All simulations were run using GROMACS 2019 [38]. Simulations were analysed using GROMACS tools and images were made using VMD [39]. Graphs were plotted using Matplotlib [40].

Acknowledgements

This work was supported by the French Infrastructure for Integrated Structural Biology (FRISBI; ANR-10- INSB-05), and the Centre National de la Recherche Scientifique (CNRS), the Agence Nationale de la Recherche and the Domaines d'Intérêt Majeur Maladies Infectieuses Région Ile de France (to MlM, CJ, GL and CM)), the Center for membrane Pumps in Cells and Disease (PUMPkin) of the Danish National Research Foundation (to JVM, PN and MB), the Lundbeck Foundation (to PN), the Wellcome Trust (ref. 220063/Z/20/Z to MMGG). We are grateful to Anna Marie Nielsen for technical support and Jesper L. Karlsen and Mark Sansom for scientific computing facilities.

Author contributions

CM carried out the yeast expression, prepared the membranes and purified protein for functional studies. GL and CM carried out tryptophan fluorescence measurements and their analysis. JDC and BA purified the protein for crystallization and prepared and harvested the crystals. MG and RAC carried out the molecular dynamics simulations and their analyses. MB collected and processed the data, refined and analysed the structure, supervised and analysed the MD simulations and wrote the paper, with contributions from all authors.

Conflict of interest

The authors declare that they have no conflict of interest.

References

1. Møller J V, Olesen C, Winther A-ML, Nissen P (2010) The sarcoplasmic Ca^{2+}-ATPase: design of a perfect chemi-osmotic pump. *Q Rev Biophys* **43**: 501–566.

2. Bublitz M, Poulsen H, Morth JP, Nissen P (2010) In and out of the cation pumps: P-Type ATPase structure revisited. *Curr Opin Struct Biol* **20**: 431–439.

3. Swarts HGP, Klaassen CHW, De Boer M, Fransen JAM, De Pont JJHHM (1996) Role of negatively charged residues in the fifth and sixth transmembrane domains of the catalytic subunit of gastric H^+,K^+-ATPase. *J Biol Chem* **271**: 29764–29772.

4. Falson P, Menguy T, Corre F, Bouneau L, Gomez De Gracia A, Soulié S, Centeno F, Møller JV, Champeil P, le Maire M (1997) The cytoplasmic loop between putative transmembrane segments 6 and 7 in sarcoplasmic reticulum Ca^{2+}-ATPase binds Ca^{2+} and is functionally important. *J Biol Chem* **272**: 17258–17262.

5. Menguy T, Corre F, Bouneau L, Deschamps S, Møller JV, Champeil P, le Maire M, Falson P (1998) The cytoplasmic loop located between transmembrane segments 6

and 7 controls activation by Ca2+ of sarcoplasmic reticulum Ca^{2+}-ATPase. *J Biol Chem* **273**: 20134–20143.

6. Zhang Z, Sumbilla C, Lewis D, Summers S, Klein MG, Inesi G (1995) Mutational analysis of the peptide segment linking phosphorylation and Ca^{2+}-binding domains in the sarcoplasmic reticulum Ca^{2+}-ATPase. *J Biol Chem* **270**: 16283–16290.

7. Menguy T, Corre F, Juul B, Bouneau L, Lafitte D, Derrick PJ, Sharma PS, Falson P, Levine BA, Møller J V., et al. (2002) Involvement of the cytoplasmic loop L6-7 in the entry mechanism for transport of Ca^{2+} through the sarcoplasmic reticulum Ca^{2+} ATPase. *J Biol Chem* **277**: 13016–13028.

8. Lenoir G, Picard M, Møller J V., le Maire M, Champeil P, Falson P (2004) Involvement of the L6–7 Loop in SERCA1a Ca^{2+}-ATPase Activation by Ca^{2+} (or Sr^{2+}) and ATP. *J Biol Chem* **279**: 32125–32133.

9. Clausen JD, Andersen JP (2004) Functional consequences of alterations to Thr247, Pro 248, Glu340, Asp813, Arg819, and Arg822 at the interfaces between domain P, M3, and L6-7 of sarcoplasmic reticulum Ca^{2+}-ATPase: Roles in Ca^{2+} interaction and phosphoenzyme processing. *J Biol Chem* **279**: 54426–54437.

10. Dyla M, Hansen SB, Nissen P, Kjaergaard M (2019) Structural dynamics of P-type ATPase ion pumps. *Biochem Soc Trans* **47**: 1247–1257.

11. Bublitz M, Musgaard M, Poulsen H, Thøgersen L, Olesen C, Schiøtt B, Morth JP, Møller JV, Nissen P (2013) Ion pathways in the sarcoplasmic reticulum Ca^{2+}-ATPase. *J Biol Chem* **288**: 10759–10765.

12. Sørensen TL-M, Møller JV, Nissen P (2004) Phosphoryl transfer and calcium ion occlusion in the calcium pump. *Science* **304**: 1672–1675.

13. Winther A-ML, Bublitz M, Karlsen JL, Møller J V, Hansen JB, Nissen P, Buch-Pedersen MJ (2013) The sarcolipin-bound calcium pump stabilizes calcium sites exposed to the cytoplasm. *Nature* **495**: 265–269.

14. Palmgren MG, Axelsen KB (1998) Evolution of P-type ATPases. *Biochim Biophys Acta* **1365**: 37–45.

15. Marchand A, Winther AML, Holm PJ, Olesen C, Montigny C, Arnou B, Champeil P, Clausen JD, Vilsen B, Andersen JP, et al. (2008) Crystal structure of D351A and P312A mutant forms of the mammalian sarcoplasmic reticulum Ca^{2+}-ATPase reveals key events in phosphorylation and Ca^{2+} release. *J Biol Chem* **283**: 14867–14882.

16. Clausen JD, Bublitz M, Arnou B, Montigny C, Jaxel C, Møller JV, Nissen P, Andersen JP, le Maire M (2013) SERCA mutant E309Q binds two Ca^{2+} ions but adopts a catalytically incompetent conformation. *EMBO J* **32**: 3231–3243.

17. Tsunekawa N, Ogawa H, Tsueda J, Akiba T, Toyoshima C (2018) Mechanism of the E2 to E1 transition in Ca^{2+} pump revealed by crystal structures of gating residue mutants. *Proc Natl Acad Sci U S A* **115**: 12722–12727.

18. Lund S, Orlowski S, De Foresta B, Champeil P, le Maire M, Moller J V. (1989) Detergent structure and associated lipid as determinants in the stabilization of solubilized Ca^{2+}-ATPase from sarcoplasmic reticulum. *J Biol Chem* **264**: 4907–4915.

19. de Foresta B, Henao F, Champeil P (1992) Kinetic characterization of the perturbation by dodecylmaltoside of sarcoplasmic reticulum Ca^{2+}-ATPase. *Eur J Biochem* **209**: 1023–1034.

20. Clausen JD, Andersen JP (2003) Roles of Leu249, Lys252, and Leu253 in membrane

segment M3 of sarcoplasmic reticulum Ca^{2+}-ATPase in control of Ca^{2+} migration and long-range intramolecular communication. *Biochemistry* **42**: 2585–2594.

21. Shainskaya A, Schneeberger A, Apell HJ, Karlish SJD (2000) Entrance port for Na^+ and K^+ ions on Na^+,K^+-ATPase in the cytoplasmic loop between trans-membrane segments M6 and M7 of the α subunit: Proximity of the cytoplasmic segment of the β subunit. *J Biol Chem* **275**: 2019–2028.

22. Toyoshima C, Nomura H (2002) Structural changes in the calcium pump accompanying the dissociation of calcium. *Nature* **418**: 605–611.

23. Toyoshima C, Mizutani T (2004) Crystal structure of the calcium pump with a bound ATP analogue. *Nature* **430**: 529–535.

24. Toyoshima C, Nakasako M, Nomura H, Ogawa H (2000) Crystal structure of the calcium pump of sarcoplasmic reticulum at 2.6 ångstrom resolution. *Nature* **405**: 647–655.

25. Cardi D, Montigny C, Arnou B, Jidenko M, Marchal E, le Maire M, Jaxel C (2010) Heterologous expression and affinity purification of eukaryotic membrane proteins in view of functional and structural studies: The example of the sarcoplasmic reticulum Ca^{2+}-ATPase. *Methods Mol Biol* **601**: 247–267.

26. Gietz RD, Schiestl RH, Willems AR, Woods RA (1995) Studies on the transformation of intact yeast cells by the LiAc/SS-DNA/PEG procedure. *Yeast* **11**: 355–360.

27. Montigny C, Azouaoui H, Jacquot A, le Maire M, Jaxel C, Champeil P, Lenoir G (2014) Overexpression of membrane proteins in *Saccharomyces cerevisiae* for structural and functional studies: A focus on the rabbit Ca^{2+}-ATPase serca1a and on the yeast lipid “flippase” complex Drs2p/Cdc50p. In, *Membrane Proteins Production for Structural Analysis* pp 133–171. Springer New York.

28. Jidenko M, Lenoir G, Fuentes JM, le Maire M, Jaxel C (2006) Expression in yeast and purification of a membrane protein, SERCA1a, using a biotinylated acceptor domain. *Protein Expr Purif* **48**: 32–42.

29. Montigny C, Arnou B, Marchal E, Champeil P (2008) Use of glycerol-containing media to study the intrinsic fluorescence properties of detergent-solubilized native or expressed SERCA1a. *Biochemistry* **47**: 12159–12174.

30. Adams PD, Afonine P V, Bunkóczi G, Chen VB, Davis IW, Echols N, Headd JJ, Hung L-W, Kapral GJ, Grosse-Kunstleve RW, et al. (2010) *PHENIX: a comprehensive Python-based system for macromolecular structure solution.*

31. Schrodinger LLC (2010) The PyMOL Molecular Graphics System, Version 1.3r1.

32. Karlsen JL, Bublitz M (2016) How to compare, analyze, and morph between crystal structures of different conformations: The P-Type ATPase example. *Methods in Molecular Biology* **1377**:523-539.

33. Best RB, Zhu X, Shim J, Lopes PEM, Mittal J, Feig M, Mackerell AD (2012) Optimization of the additive CHARMM all-atom protein force field targeting improved sampling of the backbone φ, ψ and side-chain χ(1) and χ(2) dihedral angles. *J Chem Theory Comput* **8**: 3257–3273.

34. Lee J, Cheng X, Swails JM, Yeom MS, Eastman PK, Lemkul JA, Wei S, Buckner J, Jeong JC, Qi Y, et al. (2016) CHARMM-GUI Input Generator for NAMD, GROMACS, AMBER, OpenMM, and CHARMM/OpenMM Simulations Using the CHARMM36 Additive Force Field. *J Chem Theory Comput* **12**: 405–413.

35. Jo S, Kim T, Im W (2007) Automated Builder and Database of Protein/Membrane Complexes for Molecular Dynamics Simulations. *PLoS One* **2**: e880.

36. Parrinello M, Rahman A (1981) Polymorphic transitions in single crystals: A new molecular dynamics method. *J Appl Phys* **52**: 7182–7190.

37. Bussi G, Donadio D, Parrinello M (2007) Canonical sampling through velocity rescaling. *J Chem Phys* **126**: 014101.

38. Berendsen HJC, van der Spoel D, van Drunen R (1995) GROMACS: A message-passing parallel molecular dynamics implementation. *Comput Phys Commun* **91**: 43–56.

39. Humphrey W, Dalke A, Schulten K (1996) VMD: Visual molecular dynamics. *J Mol Graph* **14**: 33–38.

40. Hunter JD (2007) Matplotlib: A 2D graphics environment. *Comput Sci Eng* **9**: 99–104.

Figure legends

Figure 1: SERCA reaction scheme, structure and activity measurements.

A Crystal structure of SERCA E340A, depicted as cartoon. Nucleotide-binding (N) domain is shown in red, actuator (A) domain in yellow, phosphorylation (P) domain in blue, M1-2 in pink, M3-4 in brown, M5-10 in grey. AMPPCP is shown as ball-and-stick, Ca^{2+} ions as cyan spheres. Residue 340 is indicated by a green sphere.

B Schematic reaction cycle of SERCA.

C Steady-state ATPase activity of purified WT SERCA (black) or E340A mutant (red) measured with an enzyme coupled assay. WT: 3.45 +/- 0.26 µmoles ATP/mg/min (n=9); E340A: 0.86 +/- 0.22 µmoles ATP/mg/min (n=9); background (dotted line): 0.18 +/- 0.06 µmoles ATP/mg/min (n=18). 3 independent experiments were done from 2 different batches of purified protein.

D Time course of Ca^{2+} binding transition as determined by following tryptophan fluorescence changes. Each time point represents the average of several measurements (n=7 for WT and n=6 for E340A from two independent experiments).

E Magnified view of the early time points in D. Error bars correspond to the standard deviation from the mean (n=7 for WT and n=6 for E340A).

F Half-time for Ca^{2+} binding for WT SERCA and E340A. $t_{1/2}$ were determined on each individual experiment. $t_{1/2}$ are 1.6 +/- 0.6 s for WT and 4.5 +/- 1.5 s for E340A with p=0.0023 (one-tailed paired “t” test).

Figure 2: Comparison of SERCA WT (PDB 3N8G) and E340A crystal structures.

A Domain rearrangements in E340A. Superposition of E340A with WT (transparent). Inset: local changes in the region around residue 340.

B,C Polar contacts between the A-domain (yellow) and the N-(red) and P-(blue) domains in WT SERCA (B) and E340A (C).

D Local hydrogen bond network (black dashes) around residue 340 in WT SERCA.

E Local hydrogen bond network (black dashes) and hydrophobic contacts (grey dashes) around residue 340 in E340A. Grey mesh: 2*m*Fo-*D*Fc electron density map contoured at 1.0 σ**.**

Figure 3: Molecular dynamics simulations of SERCA WT (WT, PDB 3N8G), E340A and *in silico* modelled mutant E340A*is* (based on 3N8G). Data for WT are shown in gray, E340A in orange and E340A*is* in yellow. Histograms give density as an arbitrary unit on the y-axis. Vertical dotted lines and asterisks refer to reference values in respective crystal structures.

A Distribution of angles between the soluble headpiece and the transmembrane domain, measured between residues Leu13 in the A-domain and Thr86 and Leu98 in M2.

B Distance histogram between C_α atoms of Leu249 at the tip of M3 and residue 340.

C Histogram of hydrogen bonds between the A-domain and the N/P domain body.

D Distance traces between Arg833-Nε and Glu/Ala340-C_α (blue) and between Leu249-C_α and Pro824-C_α (red). Left to right: simulation runs 1-3. Top traces: WT, middle traces E340A, bottom traces E340A*is*.

E Histogram of kink angles in M1, measured between C_α atoms of Trp50, Arg63 and Val74.

F Geometry distribution at the site of ATP hydrolysis. Plotted are the angles between the O- and P_γ-atoms of the terminal P_β-O-P_γ phosphoanhydride bond of ATP and the closest carboxyl oxygen (O_δ) of Asp351 versus the distance between O_δ and P_γ. Crystal structure values are given as asterisks in gray (3N8G), orange (E340A), and green (1T5T, occluded SERCA phosphoryl transition state with ADP-AlF_x).

Expanded View Figure Legends

Figure EV1: Visualisation of MD simulation analyses of E340A conformation

A Residues used to determine the headpiece angle.

B Location of residues Glu/Ala 340 on P1 and Leu249 in M3

Figure EV2: MD simulation analysis of the L6-7 loop.

A RMSD of L6-7 over the course of the simulation

B ‘In’ (left) and ‘out’ (right) positions of Arg822

C Distance traces between Arg833-Nε and Glu/Ala340-C_α (blue) and between Leu249-C_α and Pro824-C_α (red) in E340A$_{is.}$ Left to right: simulation runs 1-3.

D Visualisation of the distance measurements between Glu/Ala 340 and Arg822 and Leu 249 and Pro824.

Figure EV3: Visualisation of MD analysis of the M1 kink, measured between residues Trp50, Arg63 and Val74.

Figure EV4: Visualisation of MD analysis of the phosphorylation site geometry.

Expanded View Movie Legends

Movie EV1: Morph between equivalent Ca_2*E*1 crystal structures of SERCA WT (PDB 3N8G) and E340A (PDB 6RB2). The inset is a zoom on the region around residue 340 (green sphere).

Movie EV2: Superposed morphs between crystal structures of Ca^{2+}-free *E*1 WT (PDB 4H1W) and Ca_2*E*1 forms of WT (PDB 3N8G, light colors) and E340A (PDB 6RB2, dark colors). The inset is a zoom on the region around residue 340 (green sphere).

Appendix Figure Legends

Appendix Figure S1:

A Coomassie blue stained SDS-PAGE of the purified SERCA WT (WT) and E340A proteins.

B SERCA1a intrinsic fluorescence changes measured with purified WT (black) or E340A (red) starting at at 105 µM Ca^{2+} followed by addition of 5 mM EGTA and 12.5 mM extra Ca^{2+}. Fluorescence intensities are given as a percentage of the fluorescence level at start. For sake of clarity, data for E340A were shifted down manually by 10%. The traces shown are the average of 4 experiments for WT and 3 experiments for E340A.

Tables

Table 1: Crystallographic data collections and refinement statistics. Values in parentheses refer to the highest resolution shell

Data collection	
Beamline	ESRF ID23-2
Space group	$P2_12_12$
Unit cell (Å, °)	a=232.90, b=126.99, c=49.81, α=β=γ=90
Wavelength (Å)	0.8729
Resolution (Å)	75-3.2 (3.3-3.2)
Number of unique reflections	25337 (2201)
Completeness (%)	99.9 (99.8)
Multiplicity	6.1 (6.2)
I/σI	10.9 (1.3)
Rmeas	0.196 (>100)
$CC_{1/2}$ in highest resolution shell	0.47
Wilson B-factor	97.8
Refinement	
Resolution (Å)	49.81-3.2
Rwork/Rfree (%)	0.21/0.26
Rmsd bond (Å)	0.009
Rmsd angle (°)	0.691
Mean B-factors ($Å^2$)	90.7
Ramachandran plot (%) Favoured/allowed/outliers	93.0/6.4/0.6

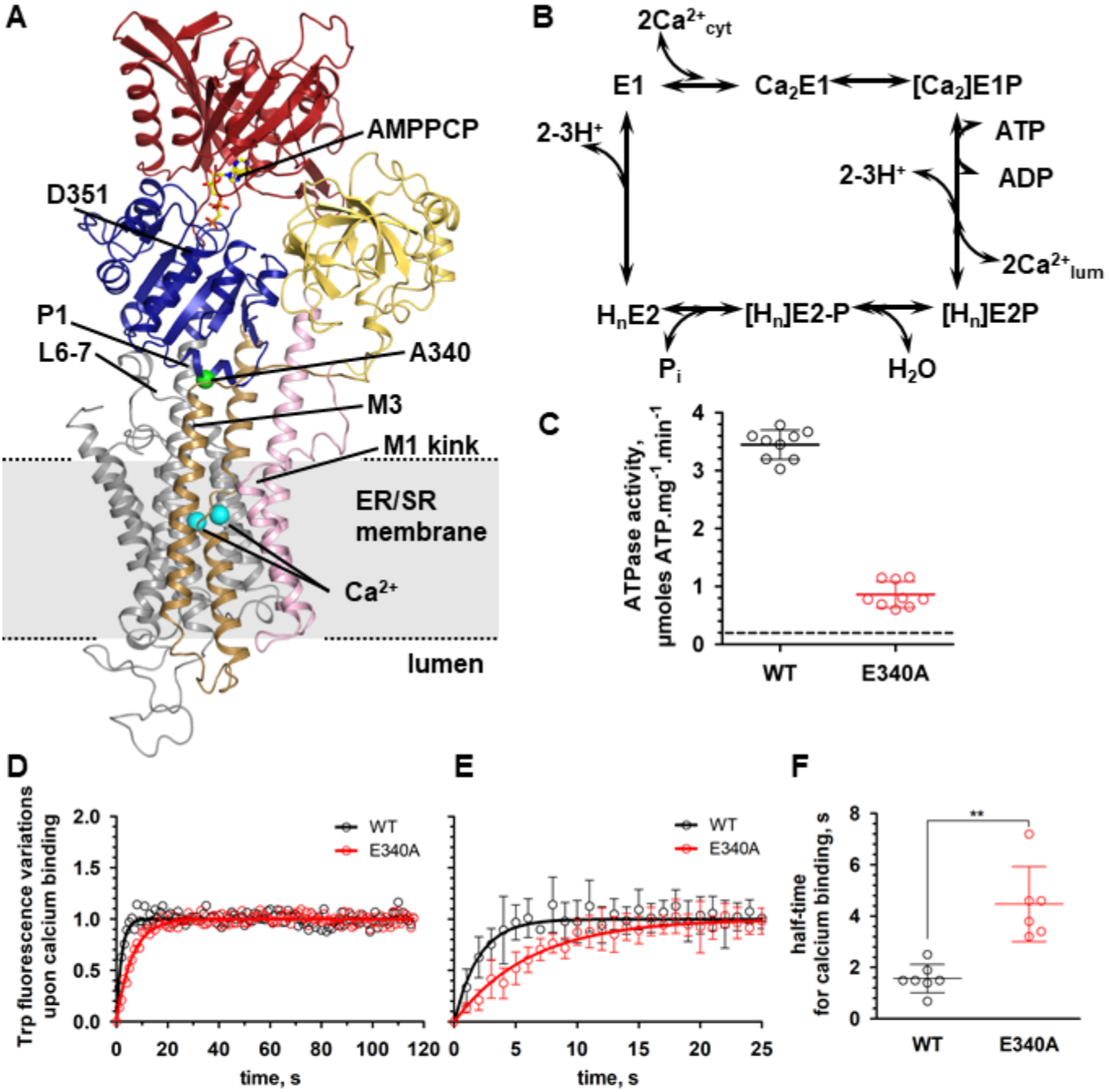

Figure 1. SERCA reaction scheme, structure and activity measurements.

A Crystal structure of SERCA E340A shown as cartoon. Nucleotide-binding (N) domain is red, actuator (A-) domain yellow, phosphorylation (P-) domain blue, M1-2 pink, M3-4 brown, M5-10 grey. AMPPCP is shown as ball-and-stick, Ca^{2+} ions as cyan spheres. Residue 340 is indicated by a green sphere.

B Schematic reaction cycle of SERCA.

C Steady-state ATPase activity of purified WT SERCA (black) or E340A mutant (red) in an enzyme coupled assay. WT: 3.45 +/- 0.26 (n=9); E340A: 0.86 +/- 0.22 (n=9); background (dashes): 0.18 +/- 0.06 (n=18). 3 independent experiments were done from 2 different batches of purified protein.

D Time course of Ca^{2+} binding transition determined by tryptophan fluorescence. Each time point represents the average of several measurements (n=7 for WT and n=6 for E340A from two independent experiments).

E Magnified view of the early time points in D. Error bars correspond to the standard deviation from the mean (n=7 for WT and n=6 for E340A).

F Half-time for Ca^{2+} binding for WT SERCA and E340A. $t_{1/2}$ were determined on each individual experiment. $t_{1/2}$ are 1.6 +/- 0.6 s for WT and 4.5 +/- 1.5 s for E340A with p=0.0023 (one-tailed paired "t" test).

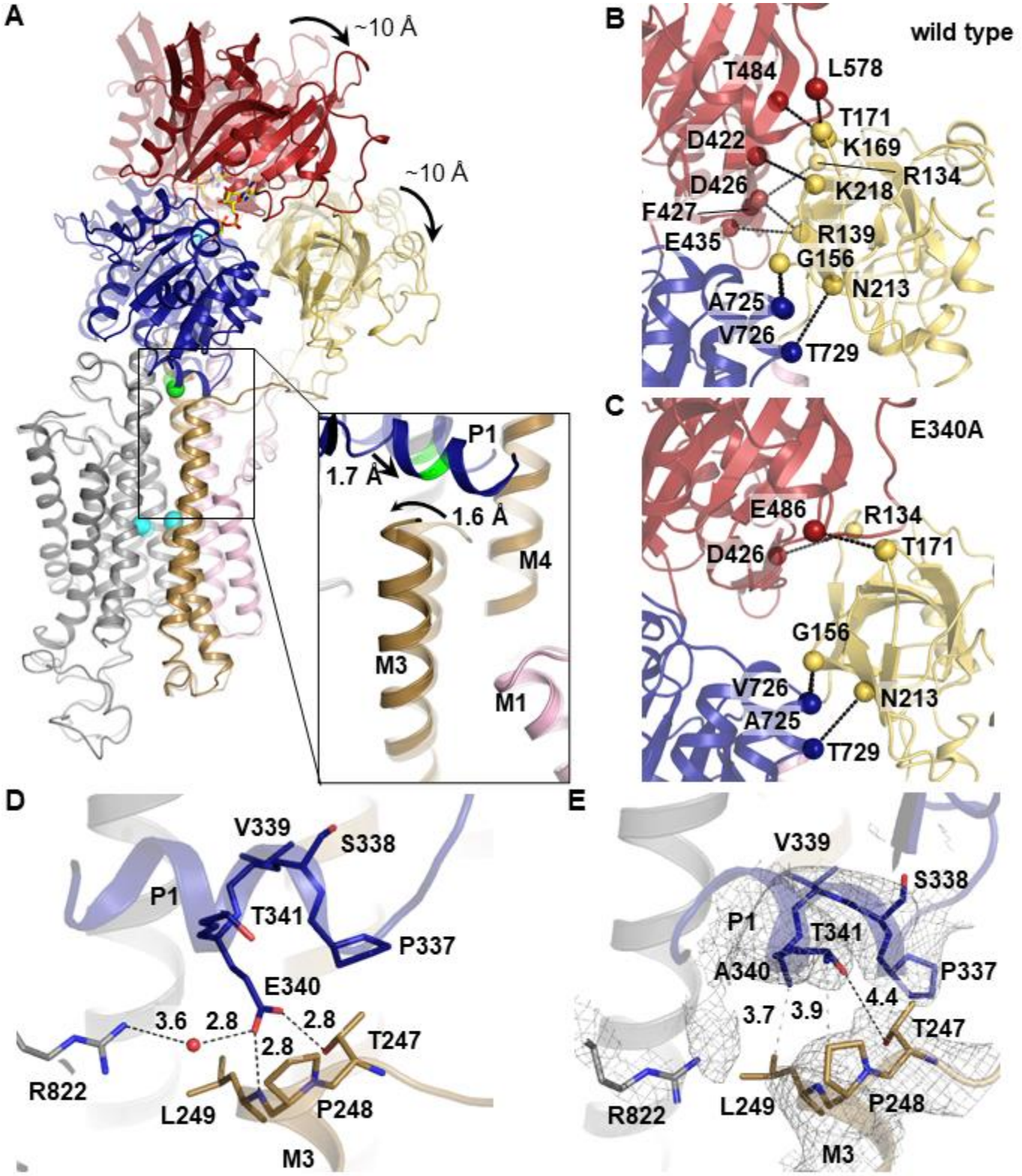

Figure 2. Comparison of SERCA WT (PDB 3N8G) and E340A crystal structures. Colouring is like in Figure 1.

A Domain rearrangements in E340A. Superposition of E340A with WT (transparent). Inset: local changes near residue 340.

B,C Polar contacts between the A-domain (yellow) and the N-(red) and P-(blue) domains in WT SERCA (B) and E340A (C).

D Local hydrogen bond network (black dashes) around residue 340 in WT SERCA.

E Local hydrogen bond network (black dashes) and hydrophobic contacts (grey dashes) around residue 340 in E340A. Grey mesh: 2*m*Fo-*D*Fc electron density map contoured at 1.0 σ.

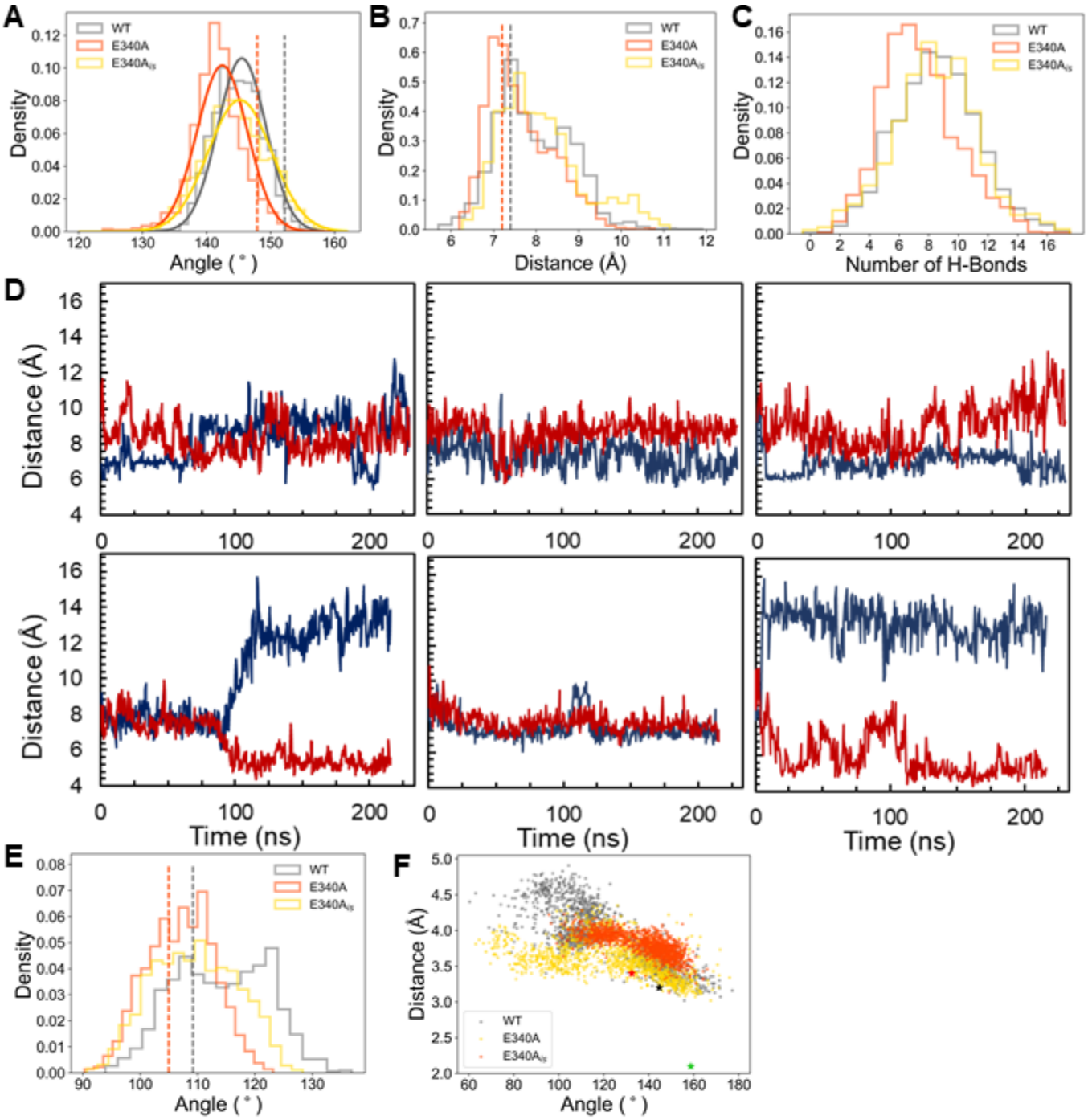

Figure 3: Molecular dynamics simulations of SERCA WT (PDB 3N8G), E340A and modelled mutant E340A$_{IS}$. WT is shown in gray, E340A in orange and E340A$_{IS}$ in yellow. Histograms give density as an arbitrary unit on the y-axis. Dotted lines and asterisks refer to reference values in respective crystal structures.

A Angle histogram between the soluble headpiece and the transmembrane domain, measured between Leu13 in the A-domain and Thr86 and Leu98 in M2.

B Distance histogram between Cα atoms of Leu249 at the tip of M3 and residue 340.

C Histogram of hydrogen bonds between the A-domain and the N/P domain body.

D Distance traces between Arg833-Nε and Glu/Ala340-Cα (blue) and between Leu249-Cα and Pro824-Cα (red). Left to right: simulation runs 1-3. Top traces: WT, bottom traces E340A.

E Histogram of kink angles in M1, measured between Cα atoms of Trp50, Arg63 and Val74.

F Geometry at the catalytic site. Angles between the O- and Pγ-atoms of the terminal phosphoanhydride bond of ATP and the closest carboxyl oxygen (Oδ) of Asp351 versus the distance between Oδ and Pγ. Green asterisk: 1T5T, ADP-AlFx complex.

Extended View Figures

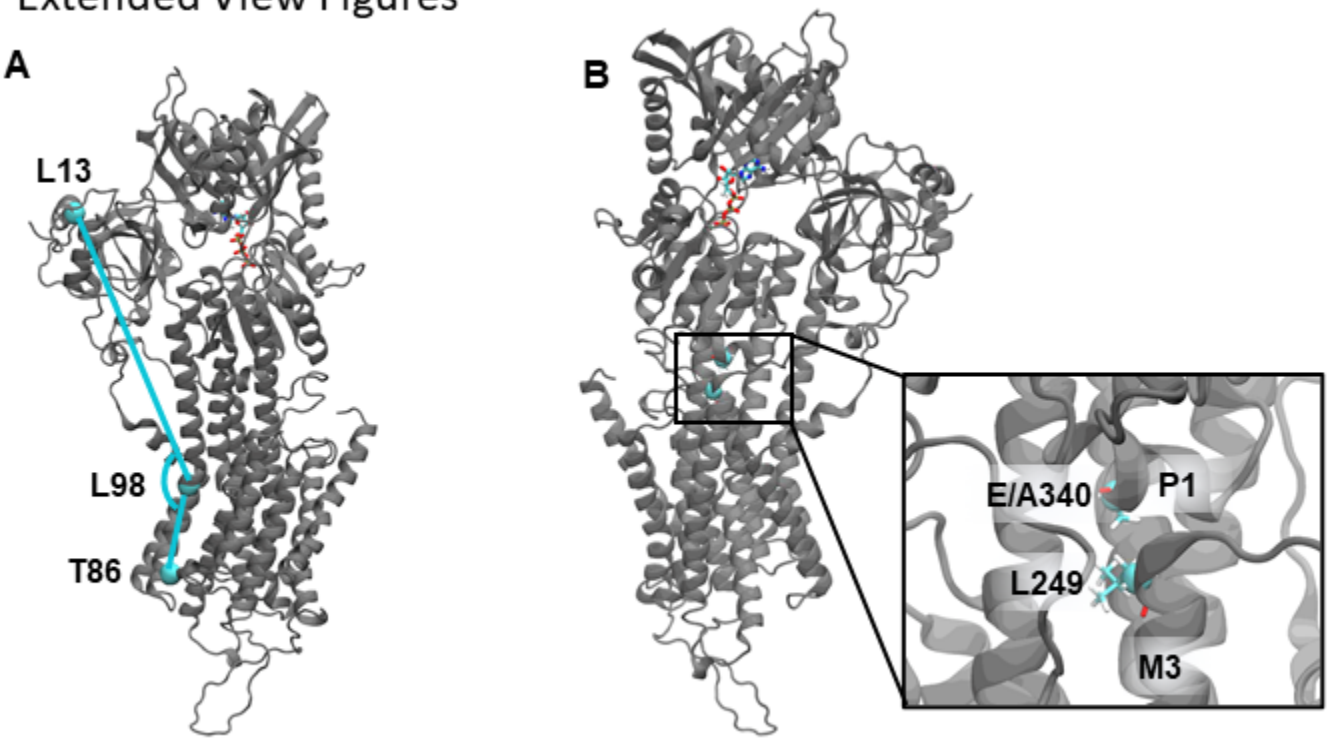

Figure EV1: Visualisation of MD simulation analyses of E340A conformation

A. Residues used to determine the headpiece angle, Leu13, Thr86 and Leu98.
B. Location of residues Glu/Ala 340 on P1 and Leu249 in M3

Extended View Figures

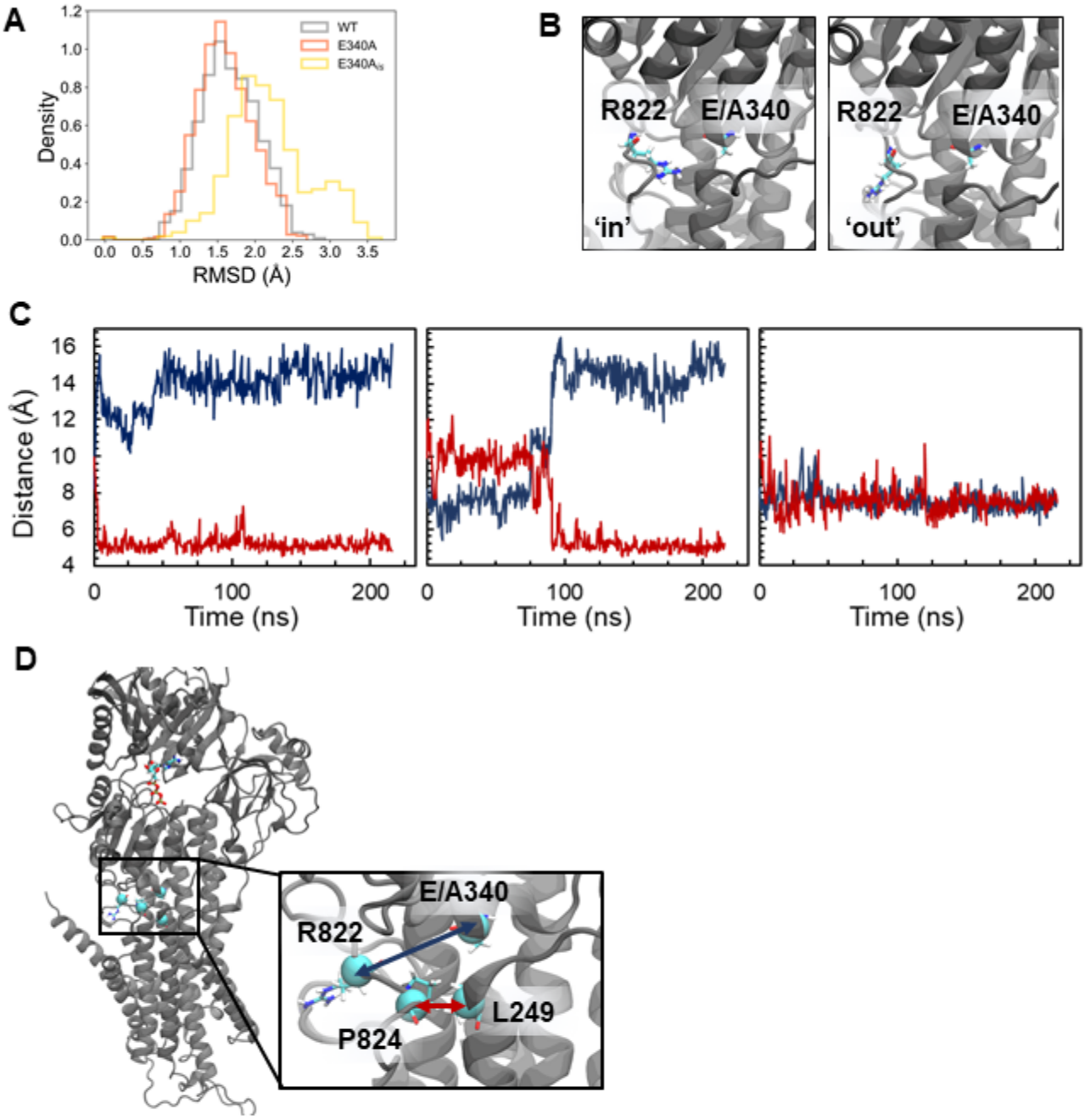

Figure EV2: MD simulation analysis of the L6-7 loop.

A RMSD histogram of L6-7 over the course of the simulation.
B 'In' (left) and 'out' (right) positions of Arg822.
C Distance traces between Arg833-Nε and Glu/Ala340-C_α (blue) and between Leu249-C_α and Pro824-C_α (red) in E340A$_{ls}$. Left to right: simulation runs 1-3.
D Visualisation of the distance measurements between Glu/Ala 340 and Arg822 and Leu 249 and Pro824.

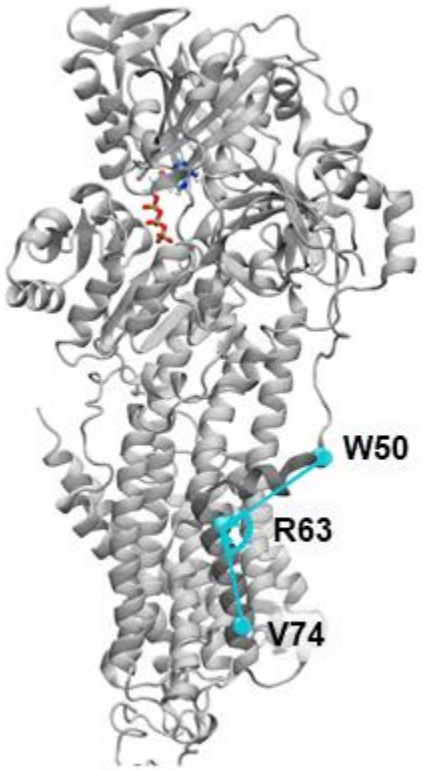

Figure EV3: Visualisation of MD analysis of the M1 kink, measured between residues Trp50, Arg63 and Val74.

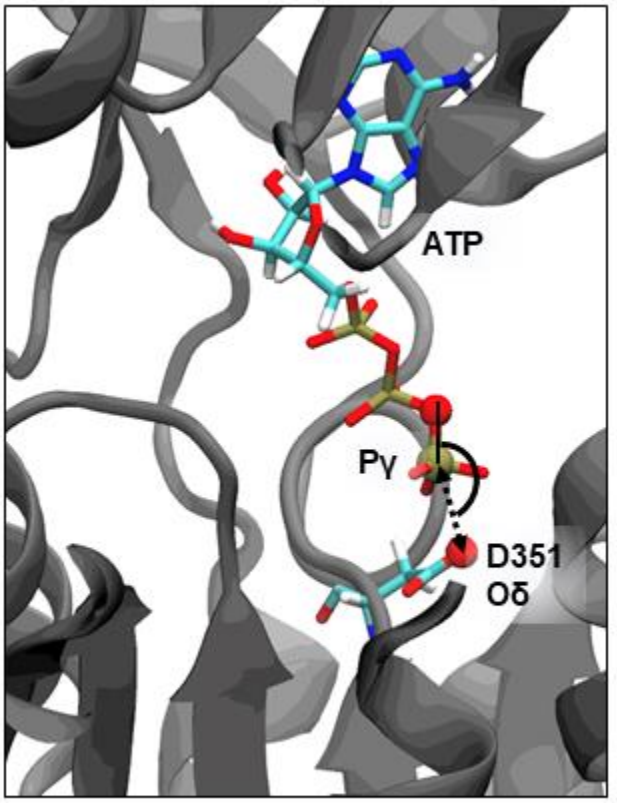

Figure EV4: Visualisation of MD analysis of the phosphorylation site geometry.

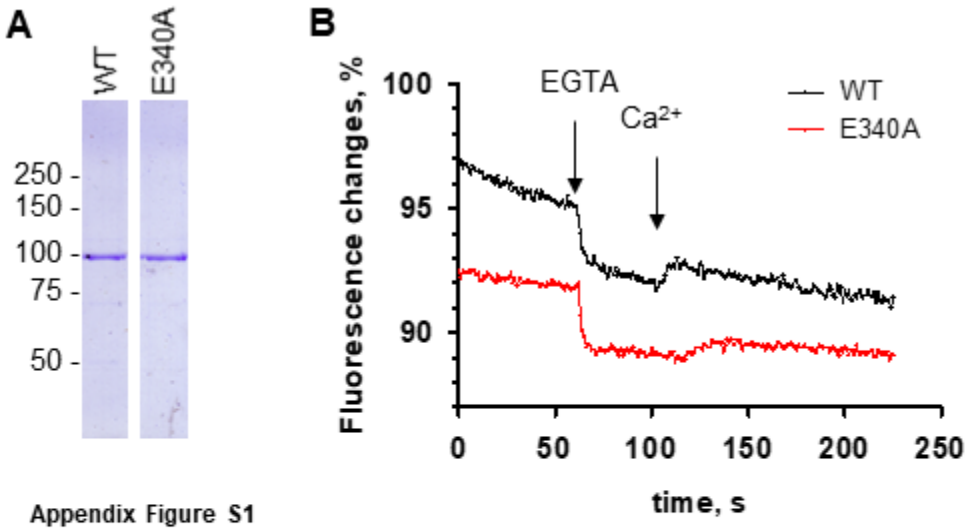

Appendix Figure S1

A Coomassie blue stained SDS-PAGE of the purified SERCA WT (WT) and E340A proteins.

B SERCA1a intrinsic fluorescence changes measured with purified WT (black) or E340A (red) starting at 105 µM Ca^{2+} followed by addition of 5 mM EGTA and 12.5 mM extra Ca^{2+}. Fluorescence intensities are given as a percentage of the fluorescence level at start. For sake of clarity, data for E340A were shifted down manually by 10%. The traces shown are the average of 4 experiments for WT and 3 experiments for E340A.